FOLWER-NORDHEIM TUNNELING IN METAL-INSULATOR-METAL VAN DER WAALS HETEROSTRUCTURES

NG SHIUAN JUN

SUPERVISOR: ASSOCIATE PROFESSOR EDA GOKI

A THESIS SUBMITTED IN PARTIAL FULFILMENT OF THE REQUIREMENTS FOR THE DEGREE OF BACHELOR OF SCIENCE WITH HONOURS

DEPARTMENT OF PHYSICS

NATIONAL UNIVERSITY OF SINGAPORE

2019

Abstract

The heterostructures of two-dimensional (2D) materials are considered promising candidates for future electronic devices. In this work, we manifest the Fowler-Nordheim (FN) tunnelling characteristics through thin layer boron nitride (BN) by fabricating metal-insulator-metal (MIM) heterostructure devices consisting of BN sandwiched by 2D metals, including few layer graphene (FLG) and high work function transition metal dichalcogenides (TMDCs): niobium disulphide (NbS_2) and tantalum disulphide (TaS_2). We argue that the main charge carrier is holes considering the band diagram of heterostructures. *I*-*V* measurements of these MIM devices show that the barrier heights for holes tunnelling through BN depend on the work function of 2D metals. The tunnelling barrier height for holes we extracted from the FN plot for TaS_2 is smaller than that of FLG, which is consistent with the expected band alignment. However, the results for NbS_2 are opposite to the prediction, which we attributed to the possible oxidation of the surface of the 2D metal. This study could provide effective ideas to modify the tunnelling features of vertical heterostructures for their prospective role in next generation high performance electronic devices.

Acknowledgements

First and foremost, I would like to express my deepest gratitude towards my supervisor, Associate Professor Eda Goki, for accepting me into his lab for my FYP. I am grateful for his guidance and ideas throughout this project. Prof Eda constantly allows us to have complete freedom to venture new ideas which gave us ample space for our personal development and has allowed me to find joy in working in the lab, fabricating new devices. Therefore, I am very honoured to be a student under him and is very thankful for the trust that he has in me.

Next, I am really grateful for my mentor, Mr Wang Jun Yong for his patience and guidance. He has patiently guided me through various phases of the project, not only teaching me how to use the various lab equipment but also taught me to remain positive even during setbacks. Despite his busy schedule, he always make it a point to check on my progress and provide necessary feedbacks. This thesis and project would not have been possible without his knowledge and guidance.

I would also like to express my gratitude towards everyone in Eda's Lab, particularly to those always in lab, for providing advices, motivation and joy through times when it was necessary. Not forgetting to mention the other FYP students under Eda's Lab, for always sharing resources and always being there for each other.

TABLE OF CONTENTS

ABSTRACT 2

ACKNOWLEDGEMENTS 3

LIST OF TABLES 5

LIST OF FIGURES 5

1. INTRODUCTION 6
    1.1 2D MATERIALS 6
    1.2 TUNNELLING THROUGH AN INSULATOR 8
    1.3 TUNNELLING THROUGH 2D MATERIALS 9
    1.4 MOTIVATION 11

2. METHODOLOGY 14

3. RESULTS AND DISCUSSION 17
    3.1 CHARACTERIZATION – RAMAN SPECTROSCOPY 17
    3.2 CHARACTERIZATION – ATOMIC FORCE MICROSCOPY (AFM) 18
    3.3 *I-V* CHARACTERISTICS 19

4. CONCLUSION 26

REFERENCES 27

List of Tables

Table 1 Comparison of observed Raman shift peak frequencies for exfoliated TaS_2 and NbS_2 against literature. 18

Table 2 Barrier height for holes ϕ_{Bh} and for electrons ϕ_{Be} calculated from FNT in MIM devices 21

List of Figures

Figure 1 Band diagram illustrating the energy barrier in FN tunnelling there is (a) no applied bias (b) applied bias. Note: the dotted arrow represents the charge carrier movement. 9

Figure 2 (a) *I-V* measurements of h-BN of various thicknesses (N=layer number) Adapted[11(redo)] (b) Energy diagram in direct tunnelling regime (c) Energy diagram in FN tunnelling regime. 11

Figure 3 (a) Work function linear dependence on barrier height (b) Schematic of heterostrucure stack. Adapted[21] 12

Figure 4 Optical microscope images of (a) Gr/h-BN/Gr device (b) TaS_2/h-BN/TaS_2 device (c) NbS_2/h-BN/NbS_2 device (d) Cross-sectional schematic representation of MIM heterostructure device. 16

Figure 5 Raman Spectrum for (a) 2H-TaS2 (b) 3R-NbS2 17

Figure 6 AFM image of 7.3nm thick h-BN used as a point of reference 18

Figure 7 Current vs Voltage, *I-V* characteristics of MIM structures 19

Figure 8 FN plot derived from *I-V* curves for (a) TMDCs MIM devices (b) Graphene MIM devices 20

Figure 9 FN tunnelling diagram representing electron/hole barrier 22

Figure 10 Visual fitting of graphene (Gr) and TaS2 into extrapolated known linear regression of barrier height against work function 23

1. Introduction

The discovery of graphene in 2004 brought about by Geim and Novoselov[1] has heralded the advent of innovative 2D materials. Isolated stable, one-atom-thick 2D layers could be obtained from van der Waals solid crystals, which exhibit unique and fascinating physical characteristics as well as many innovative routes for applications. Since there is no dangling bond in the 2D layered materials, different atomically thin 2D materials can be stacked together to form van der Waals heterostructures with various functionalities. Among them, MIM tunnelling devices show promise in electronic devices with a high on-off ratio. Even though the contact between different layers in a traditional 3D heterojunctions has been investigated, the behaviour of carrier flow through 2D interfaces could be quite unconventional, which leaves us much room to explore.

1.1 2D Materials

Atomically thin 2D materials such as graphene[2,3], hexagonal boron nitride (h-BN)[4,5], and transition metal dichalcogenides[6] (TMDCs) have been intensively studied the past decade due to the capability to assemble multiple 2D materials with complementary properties into layered heterogeneous structures.

h-BN is a typical insulating layered material with a wide band gap ~6.0 eV, high thermal stability, an atomically flat surface and ideally no dangling bonds[7,8]. With a honeycomb structure based on sp^2 covalent bonds similar to graphene, bulk h-BN has first gained tremendous attention being an exceptional substrate for graphene with an atomically smooth surface. 2D h-BN in the form of few-layer crystal, has then appeared as a fundamental building block of van der Waals

heterostructures. In addition to its high dielectric strength and electrical reliability, h-BN is considered an apt choice as a tunnelling barrier[9,10].

A single graphene layer is only a one-atom-thick layer of sp^2-bonded carbon in a tightly bound honeycomb crystal structure. Layers of graphene stacked on top of each other form graphite (bulk form), with an interplanar spacing of 0.335 nanometres (nm)[8]. The separate layers of graphene in graphite are held together by van der Waals forces, which can be cleaved during exfoliation of graphene from bulk graphite.

Bulk crystals of transition metal dichalcogenides (TMDCs) have been studied for decades. A TMDC is basically made of weakly interacting stacks of 2D MX_2 where M is a transition metal from groups IV, V, or VI and X is a chalcogen atom like S, Se, or Te. The 2D layered structure of MX_2 has increased attractiveness after 2D graphene came about.

Tantalum disulphide (TaS_2) is part of the TMDC family. TaS_2 composition is that of covalently bonded S–Ta–S planes that stack upon each other. It exists as a variety of polytypic phases that comes from the distinct in-plane Ta coordination spheres attached to S^{2-} ligands and by the stacking periodicity of individual planes. For example, the 1T and 2H polytypes unit cells exists in the form of one octahedral and two trigonal bi-pyramidal Ta-coordinated layers, respectively. Although previously it was extensively researched upon in the 1960s, 1T and 2H polytypes are once again attracting major attention as they constitute ideal case studies for the investigation of namely superconductivity[11] and charge density waves (CDW)[12].

Bulk NbS_2 is not only known for its high work function but also for its superconductivity at low temperature. The 2H-TaS_2 polytype layer structure is a known metal at ambient conditions[13].

Unlike the honeycomb crystal structure of graphene, NbS_2 have layers of trigonal edge-sharing prisms stacked onto each other. However, similar to graphene, the intra-layer bonding is primarily covalent, whereas the sheets of layers are connected by van der Waals forces. Same as TaS_2, there exists different stacking configurations of NbS_2 layers which to the formation of two polytypes - hexagonal 2H-NbS_2 with two NbS_2 layers and rhombohedral 3R-NbS_2 with three layers per unit cell[14]. The 3R polymorph layer structure causes a strong anisotropy in the physical properties like resistivity and compressibility and is a metal at ambient conditions[15].

1.2 Tunnelling through an insulator

Field electron emission is centred on free electrons tunnelling through the surface barrier by having a strong applied electric field to reduce the barrier's height and width. The first scientific explanation of field emission was proposed by Fowler and Nordheim in 1928 using the concept of quantum tunnelling and is now widely known as the Fowler-Nordheim (FN) Law[16]:

$$J_{FN}(V) = \frac{Ae^3}{8\pi h\phi_B}\frac{m}{m^*}\left(\frac{V}{d}\right)^2 exp\left(-\frac{8\pi\sqrt{2m^*}\phi_B^{\frac{3}{2}}}{3he}\frac{d}{V}\right) \quad (1)$$

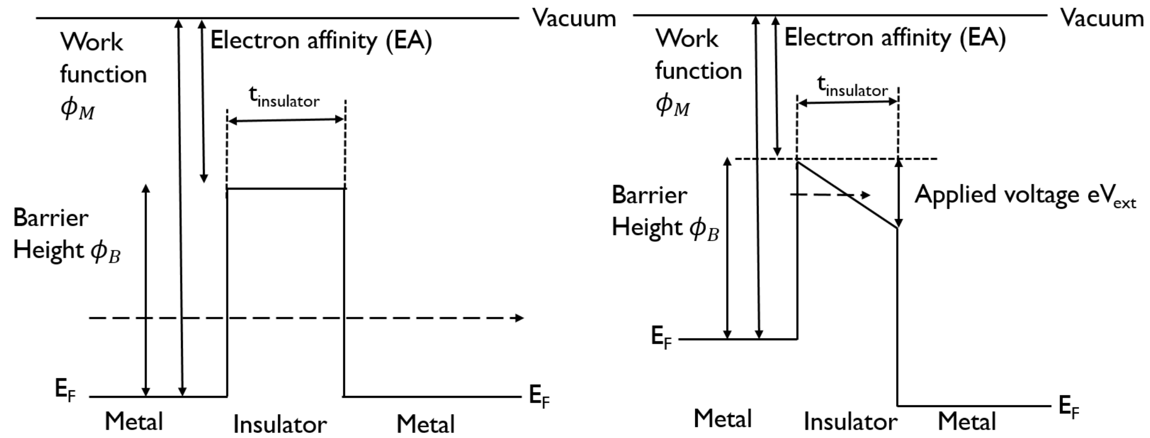

Figure 1 Band diagram illustrating the energy barrier in FN tunnelling there is (a) no applied bias (b) applied bias. Note: the dotted arrow represents the charge carrier movement.

where J_{FN}, A, ϕ_B, e, m, m*, d, and h, are field-emission current density, effective contact area, barrier height, electron charge, free electron mass, effective electron mass, barrier width, and Planck's constant respectively. This quantum mechanical tunnelling process is imperative in the study of thin barriers such as those in metal-insulator junctions. There is another kind of tunnelling that can occur across an insulator which is direct tunnelling – it occurs when the electrons tunnel through when the barrier width is small and applied bias is low. Figure 1 left diagram represents the charge carrier tunnelling that could occur without bias which is a representation of direct tunnelling where electrons tunnel through without the aid of a field. While the diagram on the right represents FN tunnelling where the barrier height is effectively pulled down by an electric field (applied voltage) to assist in charge carrier injection through the insulator.

1.3 Tunnelling through 2D Materials

The interfaces in 2D materials are different from the 3D situation due to the disparate nature of the contacts. As a typical example, in 2D materials and their interfaces, Fermi-level pinning plays a significant role compared with 3D interfaces. Within a metal/semiconductor contact, the

wavefunction of an electron at the interface of the contact must match[17]. Since the Fermi levels of the two materials must match at the interface, metal induced gap states (MGIS) arising from direct chemical bonding or surface states must exist[18]. These highly dense states would then be able to take in a large amount of charge from the metal, effectively shielding the semiconductor from the influence of the metal. As a result, the semiconductor's bands would unavoidably align to a location relative to the surface states (band bending) which are essentially pinned to the Fermi level (due to their high density), all without influence from the metal. In the typical 3D metal-2D semiconductor interface, the conductance of 2D semiconductors, MoS_2 for example, can rarely be tuned by the work function of the 3D metals[19]. This raises a question, would the carrier in the interface of a 2D metal and 2D insulator follow the band diagram or have a similar pinning effect.

As mentioned before, there are two main types of quantum tunnelling process when considering tunnelling through a 2D insulator at room temperature - direct tunnelling and Fowler-Nordheim tunnelling. However, as we are considering the 2D plane where the charge carrier injection into the insulator is travelling across a short distance, the thickness of the insulator affects whether direct or FN tunnelling dominate, illustrated in Figure 3. A very thin h-BN would result in direct tunnelling to be observed instead of FN tunnelling. In order to examine FN tunnelling explicitly, it is thus important that we have control over the thickness of the 2D insulator. For instance, it has been reported that mono-, bi- and tri-layer h-BN displays direct tunnelling current in the low-bias regime while h-BN of 4 layers and more displays FN tunnelling characteristics[20]. This phenomena can be easily explained with the diagrams in Figure 2(b) and 2(c) where the barrier width becomes so thin such that the FN tunnelling becomes insignificant and direct tunnelling of charge carriers occur instead.

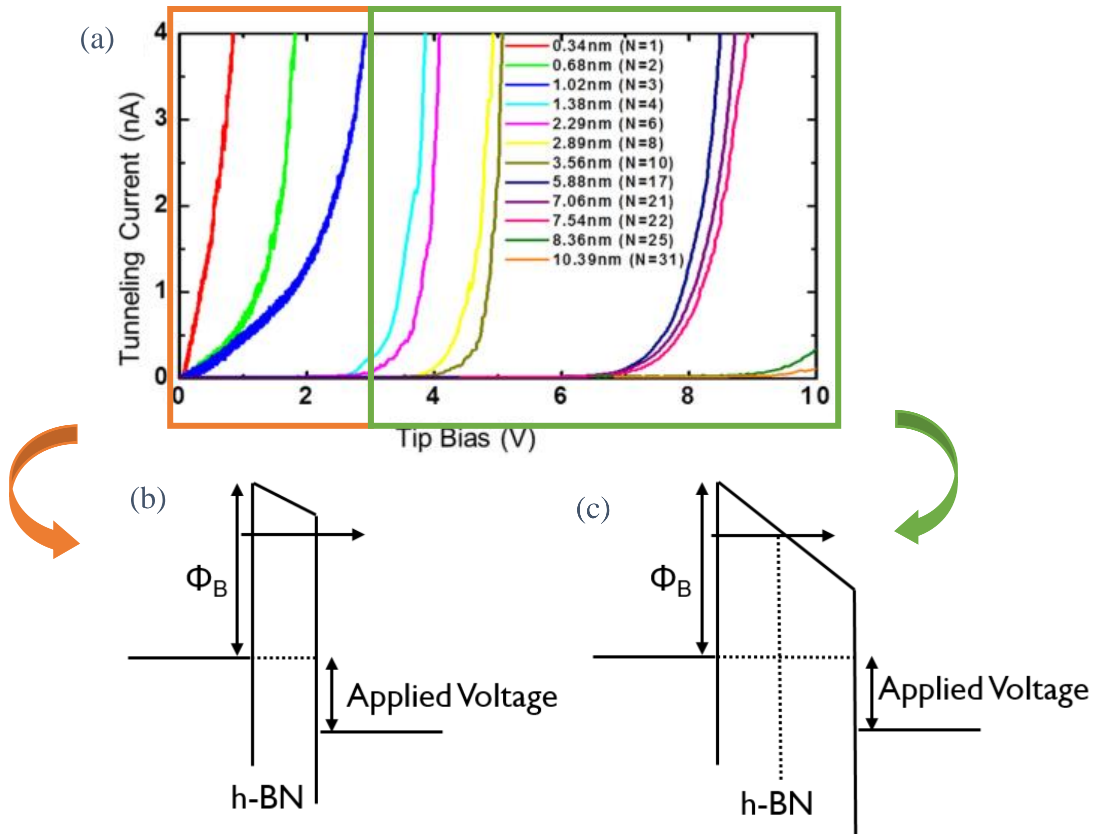

Figure 2 (a) I-V measurements of h-BN of various thicknesses (N=layer number) Adapted[20] (b) Energy diagram in direct tunnelling regime (c) Energy diagram in FN tunnelling regime.

1.4 Motivation

Recent works on modelling the electron emission from graphene has shown evidence that the Schottky barrier height of various graphene/semiconductor-based Schottky contacts is found to exhibit a strong correlation with the work function for a 2D semiconductor[21,22]. The Schottky barrier height is dependent on the atomic reactions happening at the metal/semiconductor interface as atomic orbits belonging to the metal and semiconductors are hybridized or overlapped to some degree[22]. The effect of Fermi-level pinning in metal/semiconductor contact is likely to be suppressed and hence the Schottky barrier height can be characteristically identified by the work

function of 2D semiconductor for a given metal[23–25]. It would then seem interesting to look into the dependence of barrier height on the work function of metal in 2D heterojunction contacts.

Thin film MIM tunnel devices have become a vital part in the design of integrated nano-components for a diversity of high-speed applications such as hot electron transistors[26–28] and optical rectenna for infrared energy harvesting in solar cell technology[9,29]. The classic way to attain high-speed rectification in a MIM tunnelling device is through charge transport dominated by FN tunnelling in conjunction with the use of metal electrodes with differing work functions which produce asymmetric, polarity dependent charge carrier tunnelling barriers[30].

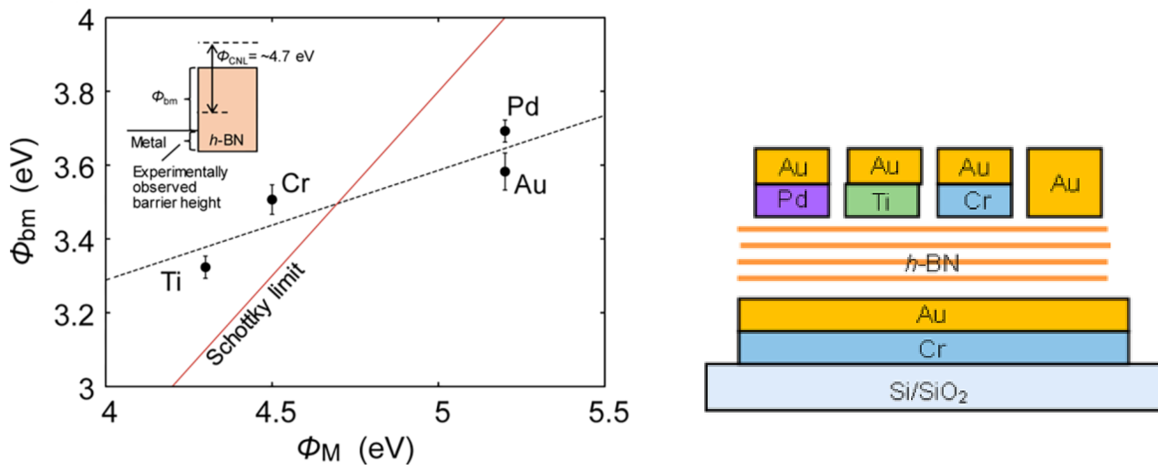

Figure 3 (a) Work function linear dependence on barrier height (b) Schematic of heterostrucure stack. Adapted [23]

Hattori and Nagashio published a recent paper on FN tunnelling through MIM devices on pure evaporated metals and they have established the existence of Fermi level pinning effect at the h-BN/metal interface[23]. Moreover, as shown from Figure 3 above, their group has identified that there is a barrier height linear correlation to the work function of metal for 4 different metal/h-BN contacts, presenting that a metal with a higher work function has a higher barrier height in FN tunnelling through h-BN. However, more has to be analysed to make a conclusive statement, especially with the case of 2D metallic TMDCs which have a different interface states when paired with h-BN[31,32]. This inspires our work to investigate the FN tunnelling model barrier height

dependence on the work function of 2D metallic TMDCs, especially high work function 2D metallic TMDCs.

2. Methodology

For the first step in the fabrication of these MIM heterostructures, h-BN graphene, NbS_2 and TaS_2 were first mechanically exfoliated from bulk single crystals onto separate Si/SiO_2 wafers. Prior to exfoliation, NbS_2 and TaS_2 were grown using the chemical vapour transport technique[33,34] where stoichiometric M (either Nb or Ta) and S is sealed in a quartz tube and heated at elevated temperatures for 10–14 days to create the bulk crystals. As the TMDCs have different existing crystalline phases where they could exhibit semiconductor or metallic properties, they were first characterized using room temperature Raman spectroscopy to determine its crystalline phase to ascertain if the exfoliated 2D material is indeed in the metallic phase as desired – 3R-NbS_2 and 2H-TaS_2.

As FNT takes place noticeably at high bias voltages whereby an increase in the barrier height could be a result of increasing interlayer film thickness of h-BN[20], it was necessary to screen the h-BN samples for a benchmark uniform thickness to be used throughout all MIM devices. Hence, samples of thin h-BN flakes, with slightly differing opacity of blue when seen under the optical microscope, had their thickness measured using Atomic Force Microscopy (AFM) - tapping mode. Through optical contrast and visual analysis[4], we were able to distinguish and categorize the thickness of h-BN flakes depending on their subtle colour differences.

To construct the 3 layered heterostructure, the pick-up dry transfer method[35] was used. A layer of polypropylene carbonate (PPC) was spin-coated on a polydimethylsiloxane (PDMS) glass stamp, and the stamp is then attached to a micromanipulator with the PPC layer facing the Si/SiO_2 wafers containing the flakes we require for the heterostructure stack. Through the use of an optical microscope to perceive the depth, the stamp is lowered slowly till the PPC layer reaches the

vicinity of the desired flake. This movement cannot be overly fast to prevent wrinkling or buckling of the sample on contact. In order to bring the substrate to slowly contact the desired flake, slow tuning of applied heat is necessary to melt the thin layer of PPC till the desired flake is encompassed by PPC before turning off the heat. After sufficient cooling for approximately 15-20 minutes, the next step is to gently raise the micromanipulator stage and peel the PDMS stamp off the Si/SiO_2 wafers. After the top layer of the MIM heterostructure is picked up, the next layer can be picked up with the same process after aligning with the next flake using the optical microscope. The complete heterostructure can then be released onto SiO_2 by melting the PPC layer onto SiO_2 with application of high heat. Any PPC residue were then removed with acetone and isopropyl alcohol. It has to be noted that in the fabrication of our device, h-BN serves as the tunnelling barrier, hence the top and bottom metal layer must not touch each other and appropriate alignment is necessary to ensure successful device fabrication is achieved.

For our MIM tunnel devices, sacrificial poly-methyl methacrylate (PMMA) were lithographically patterned to the tri-layered heterostructure by electron beam lithography, leaving the patterned electrodes mask exposed. Cr/Au metal (10/50nm) were then deposited onto the wafer using thermal vacuum evaporation technique. For this technique, Cr and Au metal is placed in an upright crucible located at the bottom of the thermal evaporator chamber and the wafer with sacrificial PMMA is fixed at the top of the chamber. After the chamber is closed, air is pumped out to simulate a high vacuum chamber. The metal vapour then rises and the surfaces to be coated are thus facing downwards to the heated source. The sacrificial PMMA layer is then lifted off, leaving behind the Cr/Au electrodes connected to the MIM heterostructure forming our MIM devices. The electrical measurements were performed at room temperature (21-25 °C) using an *I-V* analyser in the glove box.

The final schematic of the MIM heterostructure can be seen in Figure 4 below as a graphic cross-sectional representation along with optical images of 2 graphene/h-BN/graphene, TaS_2/h-BN/TaS_2 and NbS_2/h-BN/NbS_2 heterostructure MIM devices that was fabricated for this study.

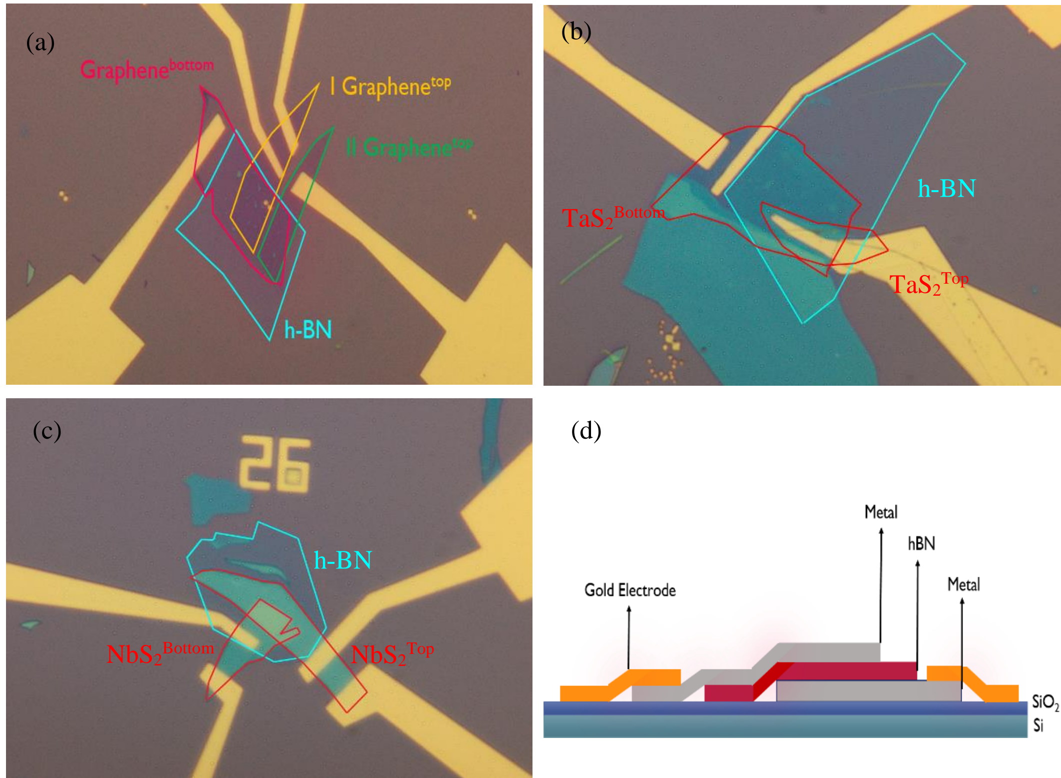

Figure 4 Optical microscope images of (a) Gr/h-BN/Gr device (b) TaS_2/h-BN/TaS_2 device (c) NbS_2/h-BN/NbS_2 device (d) Cross-sectional schematic representation of MIM heterostructure device.

3. Results and Discussion

3.1 Characterization- Raman Spectroscopy

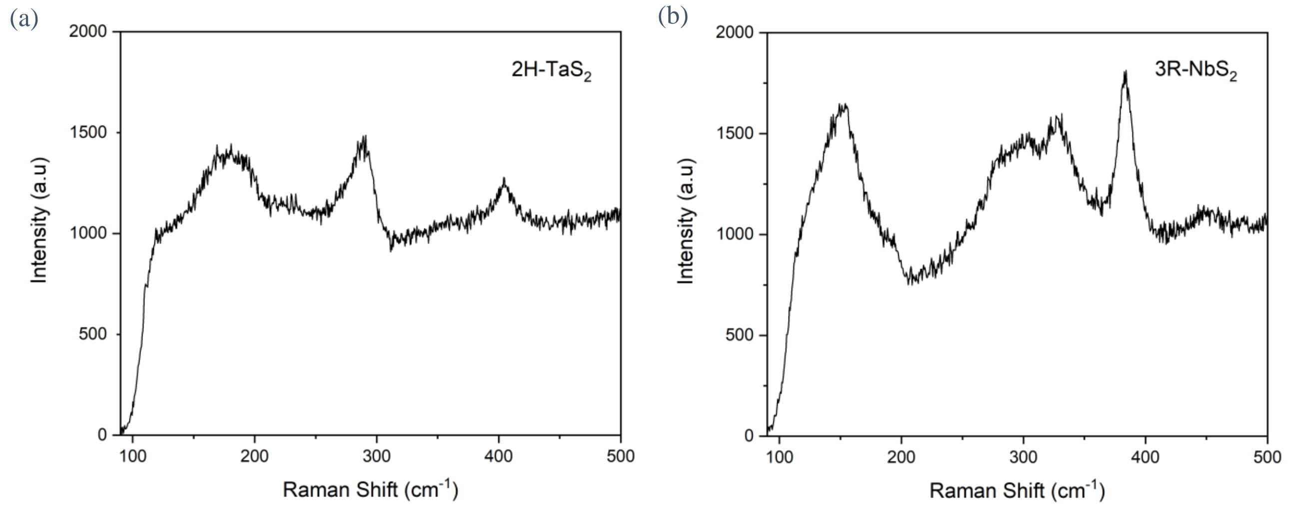

Figure 5 Raman Spectrum for (a) 2H-TaS2 (b) 3R-NbS2

Fig 5(a) and 5(b) represents the Raman spectrum obtained from our characterization of exfoliated flakes at room temperature of TaS_2 and NbS_2 respectively. The Raman scattering measurements shows Raman shift peaks of E and A modes which match well with literature results[14,36–38]. Observed peak shifts deviation from literature can be explained by the different thickness of the 2D flakes. Moreover, richness of the transition metal (Nb/Ta) could also change the strong intralayer bonding of M-X and thus change the amount by which the Raman frequency shifts[39]. Despite so, the Raman shift peaks measured strongly matches to that of other shift peaks previously known. This implies that the crystal phase of the material of exfoliated flakes is indeed in the metallic phase - 2H-TaS_2 and 3R-NbS. Table 1 below shows the data of measurements in comparison to literature.

Table 1 Comparison of observed Raman shift peak frequencies for exfoliated TaS_2 and NbS_2 against literature.

TaS_2	E^1_{2g} (cm^{-1})	E^2_{2g} (cm^{-1})	A_{1g} (cm^{-1})	A_{2g} (cm^{-1})
Raman shift peaks	-	288	197	404
Literature[11,36]	27	286	200	400
NbS_2	**E_1 (cm^{-1})**	**E_2 (cm^{-1})**	**A_1 (cm^{-1})**	**A_2 (cm^{-1})**
Raman shift peaks	294	327	382	454
Literature[14,15]	290	330	386	458

3.2 Characterization - AFM

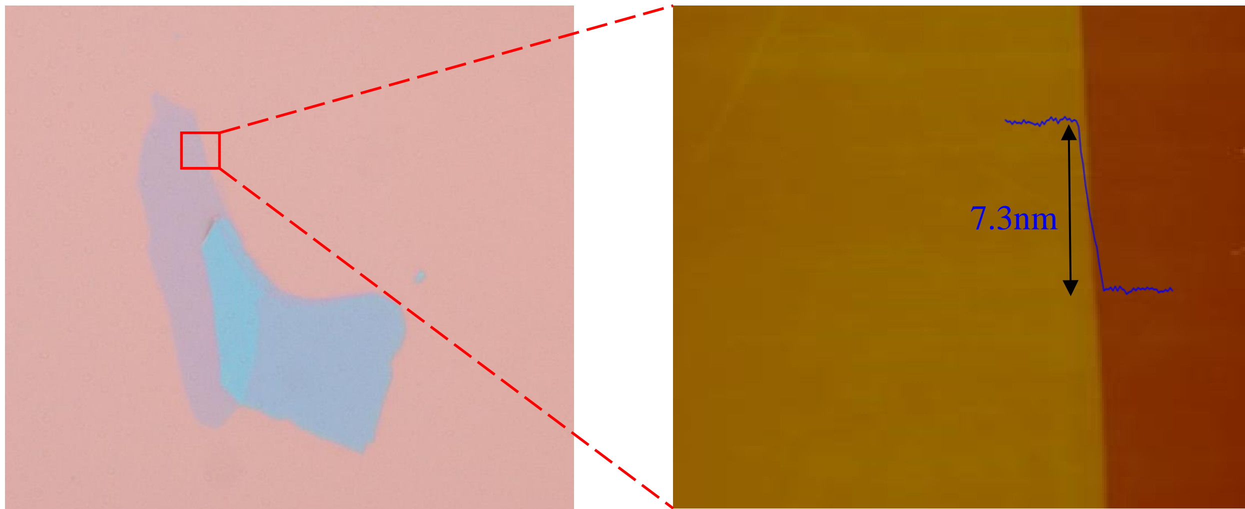

Figure 6 AFM image of 7.3nm thick h-BN used as a point of reference

AFM measurements of several exfoliated h-BN flakes of different depth of colour were taken and Figure 6 shows the benchmark optical image for 7.3nm h-BN. Visual comparison using depth of colour and opacity is used to distinguish the thickness of exfoliated h-BN on Si/SiO_2 by comparing known thickness ascertained through h-BN with new exfoliated h-BN through optical imaging. As the 7.3nm is not too thin (approximately 22 h-BN layers[4]), flakes size of 10µm and more is

relatively easy to look for under the optical microscope in 10x magnification. It is important to note that any additional layer of h-BN changes the opacity and depth of colour of the optical image of h-BN by a little and that would require a more detailed visual analysis and comparison to distinguish. Moreover, during the screening for h-BN flakes to be used, the h-BN for use should not have any form of uneven surface – which could be seen from very slight colour differences under 100x magnification optical microscope, especially between overlapping areas of the metal/insulator/metal flakes as this could undermine the intended tunnelling barrier width due to current always flowing in the path of least resistance.

3.3 *I-V* Characteristics

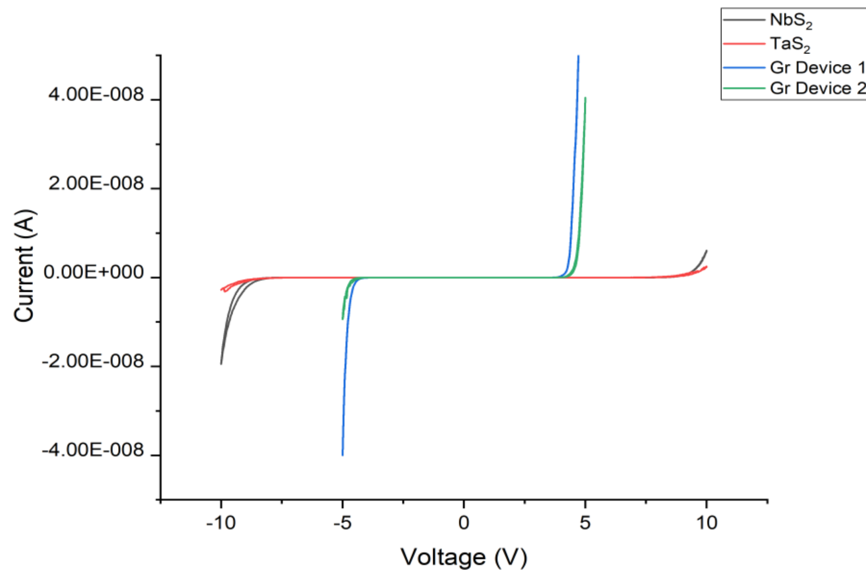

Figure 7 Current vs voltage, I-V characteristics of MIM structures

The *I-V* characteristics of the MIM devices with FLG, TaS_2 and NbS_2 were measured, with results given in Figure 7. Given the relatively large thickness (>5nm) of BN, the turn on voltage is on the high bias side given that it shows a sharp exponential increase after the turn on voltage is reached. Based on this fact, as well as from various studies, the current conduction mechanism for these

MIM structures should be FN tunnelling. However, to truly ascertain if the charge carrier transport is FN tunnelling, a FN plot for *I-V* is required – a strong linear regression in the high bias regime would indicate that FN tunnelling is dominant in the *I-V* test. Each device had both positive and negative voltages applied up to the point where FN tunnelling is observed. In the case for graphene devices, measurements were conducted in the range of -5V to 5V, whereas for the TMDCs devices, measurements were conducted in the range of -10V to 10V. All *I-V* curves of the devices demonstrate bipolar tunnelling behaviour with an asymmetric in the *I-V* curve when voltages are applied in forward and reverse bias.

In order to extract the barrier height Φ_b from our measurements, equation 1 can be rearranged to obtain a linear dependence of $ln\left(\frac{I}{V^2}\right)$ against $\frac{I}{V}$ such that a linear regression line can be plotted,

$$\ln\frac{I}{V^2} = \ln\frac{Ae^3}{8\pi h\phi_B d^2}\frac{m}{m^*} - \frac{8\pi\sqrt{2m^*}\phi_B^{\frac{3}{2}}}{3he}\frac{d}{V} \quad (2)$$

By plotting the current density divided by electric field squared (log scale) vs. the inverse of electric field across the high bias regime, the FN plot derived from the *I-V* curves can be obtained as shown in Figure 8 along with the extracted barrier heights calculated from equation 2 in forward

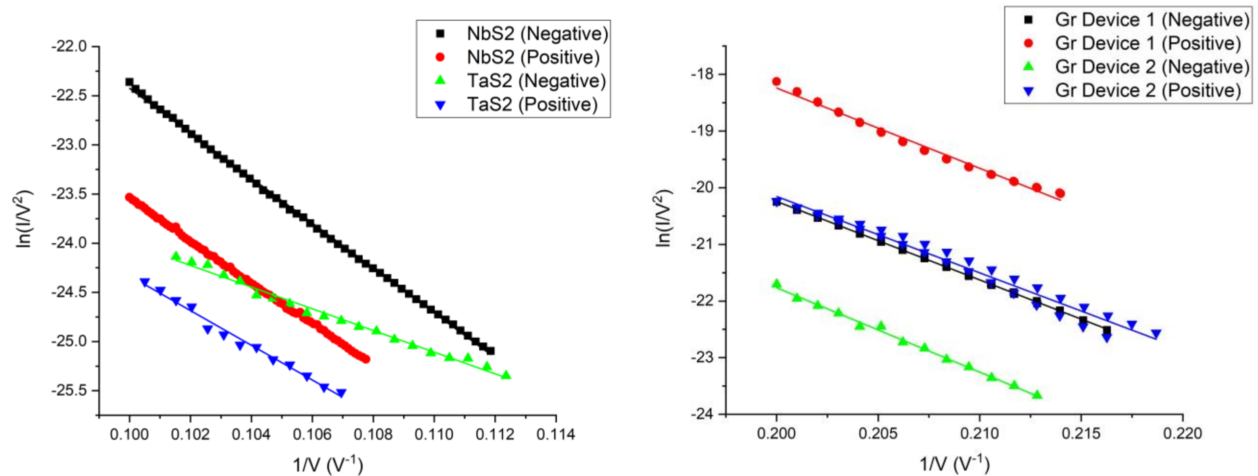

Figure 8 FN plot derived from *I-V* curves for (a) TMDCs MIM devices (b) Graphene MIM devices.

(positive bias) and reverse (negative bias) modes shown in the table below. It should be noted that the voltage values for reverse bias direction is flipped for ease of calculations.

Table 2 Barrier height for holes $\boldsymbol{\phi_{Bh}}$ and for electrons $\boldsymbol{\phi_{Be}}$ calculated from FNT in MIM devices

MIM Device	Bias Direction	ϕ_{Bh} (eV)	$\boldsymbol{\phi_{Be}}$ (eV)	R^2 (COD*)
Gr/h-BN/Gr ***Device I***	Positive	2.54	3.46	0.999
	Negative	2.58	3.42	0.989
Gr/h-BN/Gr ***Device II***	Positive	2.67	3.33	0.995
	Negative	2.50	3.50	0.971
TaS_2/h-BN/TaS_2	Positive	2.04	3.96	0.999
	Negative	2.15	3.85	0.999
NbS_2/h-BN/NbS_2	Positive	3.55	2.45	0.990
	Negative	3.48	2.52	0.987

From Figure 8 and table 2, the linear regression coefficient of determination is very close to 0.999, signifying that there is a very strong linear dependence in this plot, indicating that the tunnelling through h-BN at high bias in MIM heterostructures can be best explained by FN tunnelling model.

According to the conceptual diagram, the barrier height Φ_b for electrons can be obtained from the difference between the work function Φ_M of the metal and electron affinity of the insulator h-BN giving rise to a simple equation where, $\Phi_b = \Phi_M$ – electron affinity(h-BN). It has been reported that the main charge carrier in FN tunnelling through h-BN contact with several metals with relatively high work function (>4.2eV) is holes[23]. In this work, we assume the barrier width to be the thickness of the hBN layer, and m*/m = 0.47 for holes in h-BN[40]. The fit for Gr/h-BN/Gr, TaS_2/h-BN/TaS_2 and NbS_2/h-BN/NbS_2 devices yielded an average hole injection barrier to be 2.6

eV, 2.1eV and 3.5eV respectively. The extracted energy barrier can be modelled and predicted by finding the difference between the Fermi level of metal and valence band maximum energy of hBN.

We expect barrier height for hole injection into h-BN to be inversely dependent on work function of the metal. With the knowledge that the main charge carrier through h-BN is holes and that the bandgap of h-BN is ~6eV, we expect that the Fermi level of the metallic TMDCs to be below that of the mid gap energy of h-BN (3eV). The extracted barrier heights in Table 2 are hence for hole injections. The $\Phi_{b(electron)} = E_{g(BN)} - \Phi_{b(holes)}$ of each metal, defined as the difference in energy between the conduction band minimum of h-BN and Fermi level of the metal, is summarized with respect to the work function of the metal Φ_M.

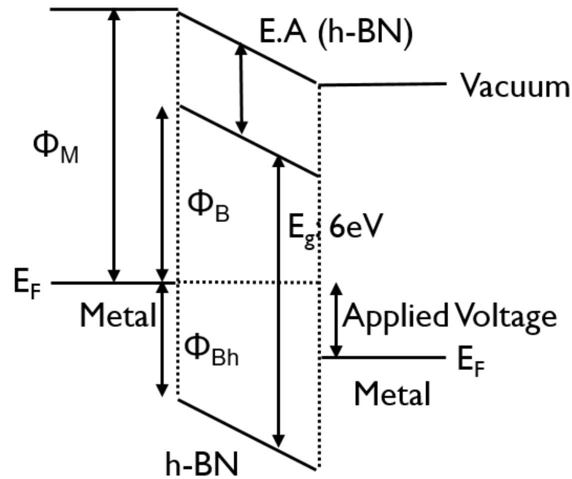

Figure 9 FN tunnelling diagram representing electron/hole barrier

Following the diagram depicted in Figure 9, a higher work function of the metal would imply a higher barrier height for electron tunnelling and a lower barrier height for hole tunnelling to occur. The theoretical work functions of graphene, TaS_2 and NbS_2 are 4.5eV[41], 5.6eV[42] and 6.22eV[43,44], respectively. The electron affinity of h-BN is approximately 1.1eV[45]. Considering that graphene has a lower work function as compared to the high work functions TMDCs, we expect that the

hole injection barrier for the TMDCs MIM devices to be lower than that of the graphene device. However, the calculations, when fitted to FN tunnelling parameters, were only conclusive for graphene and TaS_2 and not NbS_2. Following the recent work of Hattori and Nagashio as described previously, it can be seen that the average electron tunnelling barrier height $\boldsymbol{\phi_{Be}}$ for graphene and TaS_2 fits very well into their linear regression plot of barrier height against metal work function as shown in Figure 10. However, for NbS_2 which is a metallic TMDC with the highest work function to display a barrier height that is opposite from the trend requires further study.

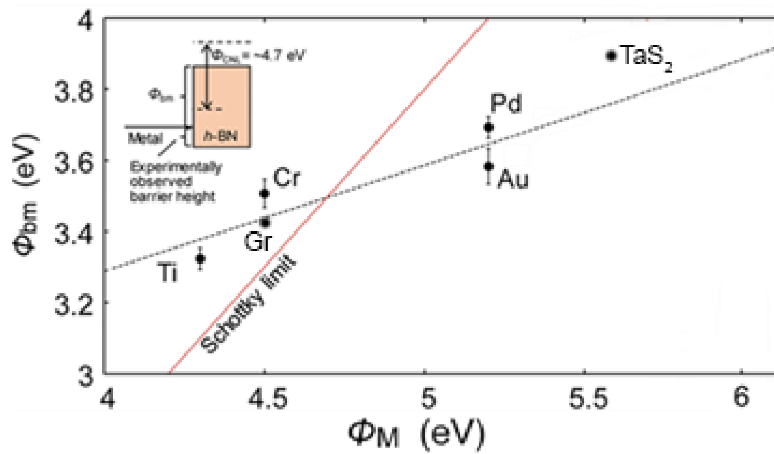

Figure 10 Visual fitting of graphene (Gr) and TaS_2 into extrapolated known linear regression of barrier height against work function

A second device of Au/h-BN/NbS_2 using the Au electrode as the top layer and NbS_2 as a second layer, the FN plot shows a tunnelling barrier of 3.18eV in the forward bias and 3.44eV in the negative bias which shows slightly better results as compared to the NbS_2/h-BN/NbS_2 device but it is still not viable in the expected trend.

The possibility that there is significant oxygen penetration into NbS_2 which may have altered the device's work function cannot be discounted. NbS_2 is known to be an unstable TMDC in ambient conditions. In fact, other groups has performed detailed transmission electron microscopy (TEM) and energy-dispersive X-ray spectroscopy (EDS) analysis on NbS_2 indicate that the NbS2 flakes prepared in air oxidize during exfoliation, evidenced by the formation of 5-7 nm of niobium oxide

sandwiching the crystalline NbS_2 layers[46]. Therefore, the transport properties in flakes below 5 nm are significantly affected by NbO_x, and the observed transport properties cannot be attributed as intrinsic to NbS2. Despite working as fast as possible from the process of exfoliation to the fabrication of the heterostructure, the formation of an oxide layer above our NbS_2 flake is inevitable. Plans to use NbS_2 flakes of relatively large thickness (>30nm) to mitigate the effect the oxide layer has proven to be ineffective too.

If we were to consider that there is an additional oxide layer sandwiching and supressing the NbS_2 metallic properties, then the FN tunnelling through h-BN would have to consider two additional layers of unknown Nb oxide. Not considering the charge transport through this oxide layer being significantly different from that of h-BN, we can conclude that the tunnelling width would significantly increase due to this oxide layer and hence making our calculations an overestimated one based on standardizing the tunnelling width to only the h-BN.

Future plans towards reassessing the barrier height dependence on the work function of NbS_2 can include constructing a 5 layer heterostructure in a glove box where oxygen content is minimal and formation of oxide layer can be slowed. A h-BN/NbS_2/h-BN/NbS_2/h-BN 5 layer heterostructure can be constructed and the outer layers of h-BN can be used as encapsulation to protect device from exposure to air when bringing it out of the glove box. This method would yield a more accurate result that would allow us to really determine if NbS_2 work function affects the barrier height across h-BN is conclusive.

It is worth noting that there is asymmetry in MIM tunnelling device. It could be due to the different thickness and surface quality of the two interfaces. It is known that graphene thickness, in the range 1-5 layers, affects its effective work function[47] which could be the cause for asymmetry in

our graphene devices. As our devices uses graphene that is approximately 2-5 layers thick, it is certainly viable to say that asymmetry could be a result of the difference in thin layers thickness.

For the TMDCs heterostructures, the most likely cause would be the surface quality of the interface. As NbS_2 is not stable in ambient conditions, the likely cause would be the interactions between the Nb oxide layer and h-BN layer that results in the asymmetry. Moreover, the fabrication process is not contamination proof, residue from the polymer used for transfer could end up on the surface of the flakes and during transfer some residue may be deposited on the interface of these devices. These contaminations can actually be seen under dark field using the optical microscope. These contaminations could be the cause for some undesired interface states that could potentially reduce the current density through the device and hence affect our results.

4. Conclusion

In this work, we manifest the FN tunnelling characteristics of several MIM heterostructure devices consisting of BN sandwiched by 2D metals (FLG, NbS_2 and TaS_2). We reason that the main charge carrier is holes considering the band diagram of heterostructures along with *I-V* measurements of these MIM devices that show that the barrier heights for holes depend on the work function of 2D metals. The tunnelling barrier height for holes we extracted from the FN plot for TaS_2 is smaller than that of FLG, which is consistent with the expected band alignment. Barrier height extracted for TaS_2 and graphene is consistent with known trend of increasing work function. Despite so, the results for NbS_2 deviates significantly from prediction, which we attribute to possible oxidation of the surface of the 2D metal. The present finding for hole injection for high work function metallic TMDCs (up to 5.6eV) provides a valid understanding carrier tunneling and transport mechanism in MIM 2D heterostructures.

References

1. Novoselov, K. S. *et al.* Electric field effect in atomically thin carbon films. *Science* **306**, 666–9 (2004).

2. Geim, A. K. & Novoselov, K. S. The rise of graphene. *Nat. Mater.* **6**, 183–191 (2007).

3. Xu, M., Liang, T., Shi, M. & Chen, H. Graphene-Like Two-Dimensional Materials. *Chem. Rev.* **113**, 3766–3798 (2013).

4. Golla, D. *et al.* Optical thickness determination of hexagonal boron nitride flakes. *Appl. Phys. Lett.* **102**, 161906 (2013).

5. Stenger, I. *et al.* Low frequency Raman spectroscopy of few-atomic-layer thick hBN crystals. *2D Mater.* **4**, 031003 (2017).

6. Manzeli, S., Ovchinnikov, D., Pasquier, D., Yazyev, O. V. & Kis, A. 2D transition metal dichalcogenides. *Nat. Rev. Mater.* **2**, 17033 (2017).

7. Zhang, K., Feng, Y., Wang, F., Yang, Z. & Wang, J. Two dimensional hexagonal boron nitride (2D-hBN): synthesis, properties and applications. *J. Mater. Chem. C* **5**, 11992–12022 (2017).

8. Wang, J., Ma, F. & Sun, M. Graphene, hexagonal boron nitride, and their heterostructures: properties and applications. (2017). doi:10.1039/c7ra00260b

9. Joshi, S. & Moddel, G. Efficiency limits of rectenna solar cells: Theory of broadband photon-assisted tunneling. *Appl. Phys. Lett.* **102**, 083901 (2013).

10. Iqbal, M. Z. & Faisal, M. M. Fowler-Nordheim tunneling characteristics of graphene/hBN/metal heterojunctions. *J. Appl. Phys.* **125**, 084902 (2019).

11. Navarro-Moratalla, E. *et al.* Enhanced superconductivity in atomically thin TaS2. *Nat. Commun.* **7**, 11043 (2016).

12. Tsen, A. W. *et al. Structure and Control of Charge Density Waves in Two-Dimensional 1T-TaS 2*.

13. Grant, A. J., Griffiths, T. M., Yoffe, A. D. & Pitt, G. D. Pressure-induced semimetal-metal and metal-metal

transitions in 1T and 2H TaS_2. *J. Phys. C Solid State Phys.* **7**, L249–L253 (1974).

14. McMullan, W. G. & Irwin, J. C. Raman scattering from 2H and 3R–NbS2. *Solid State Commun.* **45**, 557–560 (1983).

15. Ehm, L., Knorr, K. & Depmeier, W. The high-pressure behaviour of 3R-NbS2. *Zeitschrift für Krist. - Cryst. Mater.* **217**, 522–524 (2002).

16. Fowler, R. H. & Nordheim, L. Electron Emission in Intense Electric Fields. *Proc. R. Soc. A Math. Phys. Eng. Sci.* **119**, 173–181 (1928).

17. Monch, W. On the physics of metal-semiconductor interfaces. *Reports Prog. Phys.* **53**, 221–278 (1990).

18. Mönch, W. Barrier Heights of Metal Contacts on H-Terminated Diamond: Explanation by Metal-Induced Gap States and Interface Dipoles. *Europhys. Lett.* **27**, 479–484 (1994).

19. Liu, Y., Stradins, P. & Wei, S.-H. Van der Waals metal-semiconductor junction: Weak Fermi level pinning enables effective tuning of Schottky barrier. (2016). doi:10.1126/sciadv.1600069

20. Lee, G.-H. *et al.* Electron tunneling through atomically flat and ultrathin hexagonal boron nitride. *Appl. Phys. Lett.* **99**, 243114 (2011).

21. Ang, Y. S., Liang, S.-J. & Ang, L. K. Theoretical modeling of electron emission from graphene. *MRS Bull.* **42**, 505–510 (2017).

22. Liang, S.-J., Hu, W., Bartolomeo, A. Di, Adam, S. & Ang, L. K. *A modified Schottky model for graphene-semiconductor (3D/2D) contact: A combined theoretical and experimental study*.

23. Hattori, Y., Taniguchi, T., Watanabe, K. & Nagashio, K. Determination of Carrier Polarity in Fowler–Nordheim Tunneling and Evidence of Fermi Level Pinning at the Hexagonal Boron Nitride/Metal Interface. *ACS Appl. Mater. Interfaces* **10**, 11732–11738 (2018).

24. Kim, C. *et al.* Fermi Level Pinning at Electrical Metal Contacts of Monolayer Molybdenum Dichalcogenides. *ACS Nano* **11**, 1588–1596 (2017).

25. Gong, C., Colombo, L., Wallace, R. M. & Cho, K. The Unusual Mechanism of Partial Fermi Level Pinning

at Metal–MoS_2 Interfaces. *Nano Lett.* **14**, 1714–1720 (2014).

26. Vaziri, S. *et al.* A Graphene-Based Hot Electron Transistor. *Nano Lett.* **13**, 1435–1439 (2013).

27. Wang, L. *et al.* One-dimensional electrical contact to a two-dimensional material. *Science* **342**, 614–7 (2013).

28. Vaziri, S. *et al.* Bilayer insulator tunnel barriers for graphene-based vertical hot-electron transistors. *Nanoscale* **7**, 13096–13104 (2015).

29. Jayaswal, G. *et al.* Optical rectification through an Al2O3 based MIM passive rectenna at 28.3 THz. *Mater. Today Energy* **7**, 1–9 (2018).

30. Shin, J. H., Yang, J. H., Heo, S. J. & Jang, J. E. Geometric effect in a vertical stack-up metal-insulator-metal tunnel diode. *AIP Adv.* **7**, 105307 (2017).

31. Ding, L. *et al.* Understanding Interlayer Coupling in TMD-hBN Heterostructure by Raman Spectroscopy. *IEEE Trans. Electron Devices* **65**, 4059–4067 (2018).

32. Hu, Z. *et al.* Two-dimensional transition metal dichalcogenides: interface and defect engineering. *Chem. Soc. Rev.* **47**, 3100–3128 (2018).

33. Cong, C. *et al.* Synthesis and Optical Properties of Large-Area Single-Crystalline 2D Semiconductor WS_2 Monolayer from Chemical Vapor Deposition. *Adv. Opt. Mater.* **2**, 131–136 (2014).

34. Ubaldini, A. & Giannini, E. *Improved chemical vapor transport growth of transition metal dichalcogenides*.

35. Pizzocchero, F. *et al.* The hot pick-up technique for batch assembly of van der Waals heterostructures. *Nat. Commun.* **7**, 11894 (2016).

36. Sugai, S., Murase, K., Uchida, S. & Tanaka, S. Studies of lattice dynamics in 2H-TaS2 by Raman scattering. *Solid State Commun.* **40**, 399–401 (1981).

37. Zhao, R. *et al.* Two-dimensional tantalum disulfide: controlling structure and properties via synthesis. *2D Mater.* **5**, 025001 (2018).

38. Wang, D., Zhang, X. & Liu, H. Two-dimensional metallic NbS 2 : growth, optical identification and

transport properties Related content Epitaxial growth of HfS2 on sapphire by chemical vapor deposition and application for photodetectors. (2016). doi:10.1088/2053-1583/3/2/025027

39. Dash, J. K., Chen, L., Dinolfo, P. H., Lu, T.-M. & Wang, G.-C. A Method Toward Fabricating Semiconducting 3R-NbS 2 Ultrathin Films. (2015). doi:10.1021/acs.jpcc.5b04057

40. Xu, Y.-N. & Ching, W. Y. Calculation of ground-state and optical properties of boron nitrides in the hexagonal, cubic, and wurtzite structures. *Phys. Rev. B* **44**, 7787–7798 (1991).

41. Leenaerts, O., Partoens, B., Peeters, F. M., Volodin, A. & Van Haesendonck, C. The work function of few-layer graphene. *J. Phys. Condens. Matter* **29**, 035003 (2017).

42. Shimada, T., Ohuchi, F. S. & Parkinson, B. A. Work Function and Photothreshold of Layered Metal Dichalcogenides. *Jpn. J. Appl. Phys.* **33**, 2696–2698 (1994).

43. Terrones, H. & Terrones, M. Electronic and vibrational properties of defective transition metal dichalcogenide Haeckelites: new 2D semi-metallic systems. *2D Mater.* **1**, 011003 (2014).

44. Farmanbar, M. & Brocks, G. *Ohmic contacts to 2D semiconductors through van der Waals bonding*.

45. Fiori, G., Betti, A., Bruzzone, S. & Iannaccone, G. Lateral Graphene–hBCN Heterostructures as a Platform for Fully Two-Dimensional Transistors. *ACS Nano* **6**, 2642–2648 (2012).

46. Yan, R. *et al. Evolution of superconductivity in ultrathin NbS 2*.

47. Ziegler, D. *et al.* Variations in the work function of doped single-and few-layer graphene assessed by Kelvin probe force microscopy and density functional theory. *Phys. Rev. B* **83**, 235434 (2011).